

iPTF14hls in the circumstellar medium interaction model: A promising candidate for a pulsational pair-instability supernova

LING-JUN WANG,¹ LIANG-DUAN LIU,^{2,3} WEI-LI LIN,⁴ XIAO-FENG WANG,^{4,5} ZI-GAO DAI,⁶ BING LI,¹ AND LI-MING SONG¹

¹*Astroparticle Physics, Institute of High Energy Physics, Chinese Academy of Sciences, Beijing 100049, China*

²*Institute of Astrophysics, Central China Normal University, Wuhan 430079, China;*

³*Key Laboratory of Quark and Lepton Physics (Central China Normal University), Ministry of Education, Wuhan 430079, China*

⁴*Physics Department and Tsinghua Center for Astrophysics, Tsinghua University, Beijing 100084, China*

⁵*Beijing Planetarium, Beijing Academy of Sciences and Technology, Beijing, 100044, China*

⁶*CAS Key Laboratory for Research in Galaxies and Cosmology, Department of Astronomy, University of Science and Technology of China, Hefei 230026, China*

ABSTRACT

iPTF14hls is a luminous Type II supernova (SN) with a bumpy light curve that remains debated for its origin. It maintains roughly a constant effective temperature and luminosity since discovery for about 600 days, followed by a slow decay. On ~ 1000 days post discovery the light curve transitions to a very steep decline. A spectrum taken during this steep decline phase shows clear signatures of shock interaction with dense circumstellar medium (CSM). Here we explore the possibility of iPTF14hls as an interaction-powered SN. The light curve of iPTF14hls can be fitted with wind-like CSMs. Analytic modeling indicates that iPTF14hls may have undertaken six episodes of mass loss during the last ~ 200 yr. Assuming that the 1954 eruption triggered the last mass-loss episode, the stellar-wind velocity is determined to be $40 - 70 \text{ km s}^{-1}$, depending on different models. Mass loss rates are in the range $0.4 - 3.3 M_{\odot} \text{ yr}^{-1}$. The inferred total mass of ejecta and CSMs ($M_{\text{ej}} + M_{\text{CSMs}} \simeq 245 M_{\odot}$) supports the idea that iPTF14hls may be a candidate for a (pulsational) pair-instability SN. Discovery and observations of more similar stellar explosions will help understand these peculiar SNe.

Keywords: stars: massive — supernovae: general — supernovae: individual (iPTF14hls)

1. INTRODUCTION

iPTF14hls is a nearby ($z = 0.0344$) peculiar supernova (SN) first discovered in R band on 2014 Sep. 22 UT by the Intermediate Palomar Transient Factory (iPTF) wide-field camera survey (Arcavi et al. 2017). It was classified as a Type II-P (Filippenko 1997) SN according to its spectroscopic features (Li et al. 2015). The light curves of iPTF14hls last for more than 1200 days (Sollerman et al. 2018) and are bumpy in the first 500 days since discovery. The velocities of hydrogen lines of iPTF14hls decline from 8000 km s^{-1} to 6000 km s^{-1} over 600 days, during which the iron lines (Fe II $\lambda 5169$) stay at a constant velocity of 4000 km s^{-1} . The effective temperature of iPTF14hls is roughly constant ($T \approx 6000 \text{ K}$). Spectral evolution of iPTF14hls is also very slow compared to typical SNe II-P (Arcavi et al. 2017).

After 600 days from discovery, the evolution of iPTF14hls speeds up. In particular, the light curve transitions to a very steep decline since ~ 1000 days after discovery (Sollerman et al. 2018). During this time a spectrum taken on day 1153 after discovery reveals a clear signature of shock interaction with dense circumstellar medium (CSM; Andrews & Smith 2018). Interestingly, Yuan et al. (2018) report the detection of a variable γ -ray source in the energy band 0.2 to 500 GeV, which is positionally and temporally consistent with iPTF14hls. However, it cannot be confirmed whether this γ -ray source is associated with iPTF14hls or a blazar candidate.

Several models have been proposed or discussed to interpret iPTF14hls (Andrews & Smith 2018; Chugai 2018; Dessart 2018; Soker & Gilkis 2018; Wang et al. 2018; Woosley 2018; Gofman & Soker 2019; Liu et al. 2019; Modjaz

et al. 2019; Kaplan & Soker 2020; Moriya et al. 2020; Uno & Maeda 2020). However, till now no single model is able to interpret all the observational features of iPTF14hls. The late-time spectrum of iPTF14hls exhibits a double-peak intermediate-width H α line indicating strong ejecta-CSM interaction (CSI). Together with the early bumps and the late steep decline of the light curves of iPTF14hls, Andrews & Smith (2018) proposed that variations in density structure of the CSM could explain the multiple peaks of the light curve. But they did not model the long-lived light curve of iPTF14 based on successive collisions of circumstellar shells and SN ejecta in detail. In previous studies, the CSI model has been applied to a variety of SNe with bumpy light curves (Wang et al. 2016; Liu et al. 2018; Li et al. 2020). Observations reveal that bumpy features are very common (Hosseinzadeh et al. 2021) in the light curves of superluminous SNe (SLSNe; Quimby et al. 2011; Gal-Yam 2012, 2019; Moriya et al. 2018; Inserra 2019). This indicates that mass loss of massive stars during their final evolution stages are common (Smith 2014) if the bumps in the light curves of SLSNe are caused by CSM interactions. Signatures for the presence of nearby CSMs have also been reported for several SNe II-P/II-L/IIb (Quimby et al. 2007; Gal-Yam et al. 2014; Khazov et al. 2016; Yaron et al. 2017; Hosseinzadeh et al. 2018; Rui et al. 2019; Bruch et al. 2021; Jacobson-Galán et al. 2022) by the detection of flash-ionized emission lines from dense circumstellar wind.

The CSI model is also able to produce some rapidly varying light curves that can be applied to the emerging fast blue optical transients (Tolstov et al. 2019; Wang et al. 2019b; Leung et al. 2020, 2021; Xiang et al. 2021; Gal-Yam et al. 2022; Pellegrino et al. 2022). This is also an appealing factor of the CSI model because the third peak (see Figure 1 below) in the light curve of iPTF14hls varies so rapidly that it can be fitted only by a CSM interaction or other instantaneously released energy (Wang et al. 2018; Kaplan & Soker 2020).

Based on above considerations, here we explore the possibility of interpreting iPTF14hls as a multiple interaction-powered SN. We apply the semi-analytic multiple CSI model (Liu et al. 2018) to iPTF14hls to infer its explosion energy, ejecta mass, and CSM parameters, which allow us to consider the mass-loss history of the progenitor system. The semi-analytic model is based on a spherically symmetric explosion with optically thick CSMs in spheric geometry (Chatzopoulos et al. 2012). As a result, the model predicts a stationary photosphere, inconsistent with the observed photospheric velocities. However, such a model can be improved by considering a clumpy CSM (Chugai & Danziger 1994) or an asymmetric, disk-like medium embedded within the spherically expanding ejecta (Smith 2017; Andrews & Smith 2018; Suzuki et al. 2019). The semi-analytic model is computationally efficient and can give a convenient estimate of the relevant parameters.

This paper is structured as follows. The models and fitting results are presented in Section 2. Mass loss history is derived in Section 3. Discussion and conclusions are given in Section 4.

2. MODELS AND RESULTS

2.1. CSI model

The CSI model assumes that the ejecta expand at a constant velocity v_{SN} with an inner power-law density profile ($\rho \propto r^{-\delta}$ with $\delta < 3$) surrounded by a steep outer power-law profile ($\rho \propto r^{-n}$ with $n > 5$; Parker 1961; Chevalier 1982; Chevalier & Fransson 1994). The Lagrangian coordinate for the transition from the inner flat profile to the outer steep profile is denoted as x_0 (Chatzopoulos et al. 2012). In this paper, we set $\delta = 0$, $x_0 = 0.7$.

The density profile of CSMs is also assumed in a power-law form $\rho \propto r^{-s}$. The CSM was ejected by the SN progenitor during its evolution to the final collapse. Usually two kinds of density profile of CSMs are considered, namely the stellar wind with $s = 2$ or a uniform shell with $s = 0$. In a multiple CSI model (Liu et al. 2018), we denote the mass of the i th CSM as $M_{\text{CSM},i}$. The inner radius of the i th CSM is denoted as $R_{\text{in},i}$. Similarly, the CSM density at $R_{\text{in},i}$ is denoted as $\rho_{\text{in},i}$.

Collision of the ejecta with CSM results in the formation of a forward shock (FS) propagating into CSM and a reverse shock (RS) propagating into the ejecta. The dynamical evolution of FS and RS is described by a self-similar solution (Chevalier 1982). Both FS and RS convert the kinetic energy of the homologously expanding ejecta into radiation that powers the SN light curve. Based on those self-similar solutions one can derive the expression for the FS and RS input luminosity that is produced from CSI. The input luminosities of FS and RS have the same temporal index (Chatzopoulos et al. 2012; Moriya et al. 2013b; Wang et al. 2019a)

$$L_{\text{inp,FS}}(t) = L_{\text{FS,tr}} \left(\frac{t}{t_{\text{tr}}} \right)^\alpha, \quad L_{\text{inp,RS}}(t) = L_{\text{RS,tr}} \left(\frac{t}{t_{\text{tr}}} \right)^\alpha, \quad (1)$$

where the temporal index is

$$\alpha = \frac{2n + 6s - ns - 15}{n - s}, \quad (2)$$

and t_{tr} is the characteristic time of dynamical evolution, $L_{\text{inp,FS}}$ and $L_{\text{inp,RS}}$ are the characteristic input luminosities of FS and RS, respectively. These characteristic physical quantities depend on the nature of the CSM and SN explosion, and the specific expressions are given in Liu et al. (2020). The heating from FS terminates when all the available optically thick CSM has been swept up, by which one can obtain the FS termination timescale $t_{\text{FS,*}}$. Similarly, the RS termination time $t_{\text{RS,*}}$ is determined when all the ejecta M_{ej} has been swept.

The input luminosities of FS and RS from i th CSM interaction is

$$L_{\text{inp,CSM},i,\text{FS}}(t) = \epsilon_{\text{FS},i} L_{\text{inp,FS},i}(t), \quad (3)$$

$$L_{\text{inp,CSM},i,\text{RS}}(t) = \epsilon_{\text{RS},i} L_{\text{inp,RS},i}(t), \quad (4)$$

respectively. Here ϵ_{FS} and ϵ_{RS} are the respective conversion efficiency from the kinetic energy to radiation by FS and RS. Chatzopoulos et al. (2012) assume that all kinetic energy of SN ejecta converts efficiently to radiation, that is $\epsilon_{\text{FS}} = \epsilon_{\text{RS}} = 1$. It may be reasonable for the case $M_{\text{CSM}} \gg M_{\text{ej}}$, on the contrary, this assumption is unrealistic for $M_{\text{CSM}} \ll M_{\text{ej}}$ (van Marle et al. 2010; Moriya et al. 2013a). Because of poor knowledge of the physical process of converting the kinetic energy to radiation, we set ϵ_{FS} and ϵ_{RS} as independent parameters. After traversing a CSM, the ejecta will grow in mass and collide with the next CSM. Thus, the ejecta mass of the i th interaction is

$$M_{\text{ej},i} = M_{\text{ej},i-1} + M_{\text{CSM},i-1} \quad (5)$$

Previous studies of multiple-interaction models (Liu et al. 2018; Li et al. 2020) have usually assumed that a RS develops at every shell collision. However, whether a RS develops depends on the density structure and the pre-shock pressure. For the first collision of a “cold” SN ejecta and a “cold” CSM, both FS and RS would develop. Due to the pre-heat high pressure of the first FS, in successive collisions of CSM shells, RSs do not always develop or they are at least very weak with less effective contributions to the total luminosity. Therefore, in our calculation, we only consider the contributions from FSs and the first RS and neglect the contributions from the rest RSs.

Considering the expansion velocity of the CSM is much lower than the typical velocity of the SN ejecta, a fixed photosphere inside the CSM is usually adopted (Chatzopoulos et al. 2012; Liu et al. 2018). Under this assumption, the theoretical bolometric light curves contributed by FS and RS of the i th collision are given by

$$L_{i,\text{FS}}(t) = \frac{1}{t_{\text{diff},i,\text{FS}}} \exp\left(-\frac{t}{t_{\text{diff},i,\text{FS}}}\right) \int_0^t \exp\left(-\frac{t'}{t_{\text{diff},i,\text{FS}}}\right) L_{\text{inp,CSM},i,\text{FS}}(t') dt', \quad (6)$$

$$L_{i,\text{RS}}(t) = \frac{1}{t_{\text{diff},i,\text{RS}}} \exp\left(-\frac{t}{t_{\text{diff},i,\text{RS}}}\right) \int_0^t \exp\left(-\frac{t'}{t_{\text{diff},i,\text{RS}}}\right) L_{\text{inp,CSM},i,\text{RS}}(t') dt', \quad (7)$$

respectively. Here $t_{\text{diff},i,\text{FS}}$ and $t_{\text{diff},i,\text{RS}}$ are the respective diffusion times of the FS and RS of the i th CSM. The theoretical bolometric light curve of N times interactions is given by

$$L(t) = \sum_{i=1}^N [L_{i,\text{FS}}(t) + L_{i,\text{RS}}(t)]. \quad (8)$$

After $t_{i,\text{FS,*}}$ and $t_{i,\text{RS,*}}$, luminosity input from FS and RS ceases in the CSI models, and the decline in luminosity is predicted to be exponential.

To handle the diffusion of the shock energy, different authors take different recipes. Liu et al. (2018) adopted diffusion timescale in the optically thick CSM for both FS and RS, that is

$$t_{\text{diff},i,\text{FS}} = t_{\text{diff},i,\text{RS}} = \sum_{j=i}^N \frac{\kappa_j M_{\text{CSM,th},j}}{\beta c R_{\text{ph}}}, \quad (9)$$

where N is the total number of CSMs, $\beta \simeq 13.8$ is a constant (Arnett 1982), c is the speed of light, R_{ph} is photospheric radius of the outermost CSM, κ_j , and $M_{\text{CSM,th},j} \simeq M_{\text{CSM},j}$ are the optical opacity and optically thick mass of the j th CSM. We denote recipe used in Liu et al. (2018) as CSI-L.

Wheeler et al. (2017) assume that the shocks locate in the center of the ejecta, that is, the original spirit of Arnett (1982). In this situation, the diffusion time of the i th CSI is

$$t_{\text{diff},i,\text{FS}} = t_{\text{diff},i,\text{RS}} = \frac{\kappa M_{\text{ej}}}{\beta c R_{\text{ph}}} + \sum_{i=1}^N \frac{\kappa_i M_{\text{CSM,th},i}}{\beta c R_{\text{ph}}}, \quad (10)$$

where κ is the optical opacity of the ejecta. To be distinctive, hereafter we denote the recipe in Wheeler et al. (2017) as CSI-W.

However, the FS and RS are not centrally concentrated and move within the CSM and ejecta, respectively. The assumption of a deeply located power source is approximately appropriate for the RS, but is not true for the FS. As one may expect, different recipes have different advantages and shortcomings. The CSI-W model can better handle the RS luminosity, while the CSI-L model handles the FS luminosity better. The model can be improved by combining the advantages of models CSI-L and CSI-W. We can set the diffusion time of the FS as done in the CSI-L model, while setting the diffusion time of RS as done in the CSI-W model, that is

$$t_{\text{diff},i,\text{FS}} = \sum_{j=i}^N \frac{\kappa_j M_{\text{CSM,th},j}}{\beta c R_{\text{ph}}}, \quad (11)$$

$$t_{\text{diff},i,\text{RS}} = \frac{\kappa M_{\text{ej}}}{\beta c R_{\text{ph}}} + \sum_{i=1}^N \frac{\kappa_i M_{\text{CSM,th},i}}{\beta c R_{\text{ph}}}. \quad (12)$$

Such a treatment is denoted as model CSI-LW and the Python code is available on GitHub¹ and version 1.0 is archived in Zenodo (Wang & Yu 2022).

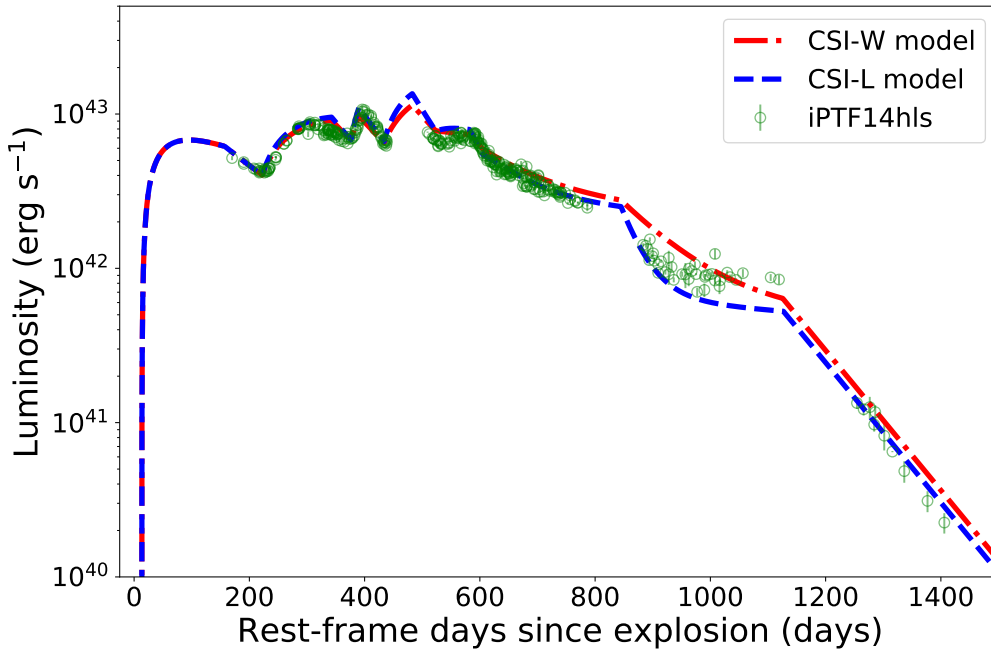


Figure 1. Fit to the bolometric luminosity of iPTF14hls by the CSI-L model and CSI-W model. The data are taken from Arcavi et al. (2017) and Sollerman et al. (2018).

¹ CatFit codebase: <https://github.com/Lingjun-Wang/CatFit>.

Table 1. Model parameters for iPTF14hls based on the pure-CSI models.

| ejecta properties | | | | | | |
|--|------|------|------|-----|------|------|
| $M_{\text{ej}}(M_{\odot})$ | 75 | | | | | |
| $v_{\text{sn}} (\text{km s}^{-1})$ | 5200 | | | | | |
| δ | 0 | | | | | |
| n | 7 | | | | | |
| CSM properties | | | | | | |
| | 1st | 2nd | 3rd | 4th | 5th | 6th |
| $M_{\text{CSM}}(M_{\odot})$ | 20 | 25.5 | 8 | 25 | 22 | 70 |
| $R_{\text{in}}(10^{15} \text{ cm})$ | 0.6 | 10 | 16 | 18 | 21 | 23.5 |
| $\rho_{\text{in}}(10^{-15} \text{ g cm}^{-3})$ | 1200 | 7.2 | 6.0 | 5.0 | 3.2 | 2.2 |
| ϵ_{FS} | 0.02 | 0.09 | 0.26 | 0.2 | 0.09 | 0.04 |
| ϵ_{RS} | 0.4 | 0 | 0 | 0 | 0 | 0 |

The comparison of the fitting results of CSI-L model and CSI-W model is given in Figure 1, and the fitting parameters are listed in the Table 1. With the same fitting parameters, the theoretical light curve of model CSI-LW is shown in Figure 2. The model parameters were varied manually until reasonable agreement between the observational data and the theoretical model was found. The initial slow decline of the light curve favors a small $n < 9$ and wind-like CSMs. So we set $n = 7$ and $s = 2$. With these values, $\alpha = -0.6$. The spike (the third peak) in the light curve at ~ 400 days after explosion can only be fitted by a CSM much lighter than the ejecta. The opacity of the ejecta and CSMs is $\kappa = 0.34 \text{ cm}^2 \text{ g}^{-1}$ (Matzner & McKee 1999), which is the Thomson electron scattering opacity for fully ionized solar metallicity material. We find that in order to get a close fit to the light curve of iPTF14hls, six wind-like CSM-shells are required. The CSI model predicts an exponential decay of the light curve after the forward shock sweeps up all the CSM or the reverse shock sweeps up all the ejecta. The exponential decay of the light curve starting from ~ 1100 days after explosion is contributed by the first RS (see Figure 1).

Given the same fitting parameters, Figure 1 shows that the theoretical light curve of CSI-L is brighter than that of CSI-W during the early phase of the light curve and becomes dimmer during late stage. This can be easily understood because the diffusion time in CSI-L is shorter and emission diffuses out earlier.

One of the most influential parameters on the theoretical light curve is the inner radius of the i th CSM $R_{\text{in},i}$, which determines the onset time of the interactions. In CSI-W, ejecta mass M_{ej} affects the maximum and the width of the light curve, higher ejecta mass leading to long-lived RS emission. The larger the CSM mass, the longer the light curve. For pure CSI model the first RS has a long duration and contributes mainly to the first peak and the late-time steep decline. The explosion energy of iPTF14hls is estimated to be (Chevalier & Fransson 1994; Chatzopoulos et al. 2012)

$$E_{\text{SN}} = \frac{(3 - \delta)(n - 3)}{2(5 - \delta)(n - 5)} M_{\text{ej}} (x_0 v_{\text{SN}})^2 = 1.2 \times 10^{52} \text{ erg}, \quad (13)$$

of which 5.5×10^{50} erg was emitted as visual light.

2.2. CSI plus ^{56}Ni model

From Table 1 we see that in the pure CSI model the progenitor has a zero-age main-sequence mass $M_{\text{zams}} \simeq M_{\text{ej}} + \Sigma M_{\text{CSMs}} \simeq 245.5 M_{\odot}$. The true value of M_{zams} may be higher than the value given here, to account for other pre-explosion mass-loss processes and the massive compact remnant, if the progenitor of iPTF14hls was not completely disrupted. For such massive stars, it is expected that some amount of ^{56}Ni is synthesized during the SN explosion (Heger & Woosley 2002; Umeda & Nomoto 2002).

In addition, in pure-CSI model the initial slow decline of the light curve can only be fitted with a CSM interaction in which the RS emission dominates over FS emission. This results in a $\epsilon_{\text{FS}} = 0.02$ exceptionally small compared to ϵ_{FS} of other CSMs. The initial decline can also be fitted with a CSM whose mass $M_{\text{CSM}} \gtrsim 20 M_{\odot}$, so that the FS emission can last for more time to have a similar time dependence as RS. This is because the heating rates of FS and RS have the same power-law index (see Equation 1). However, with such a massive CSM, it will be difficult to fit the

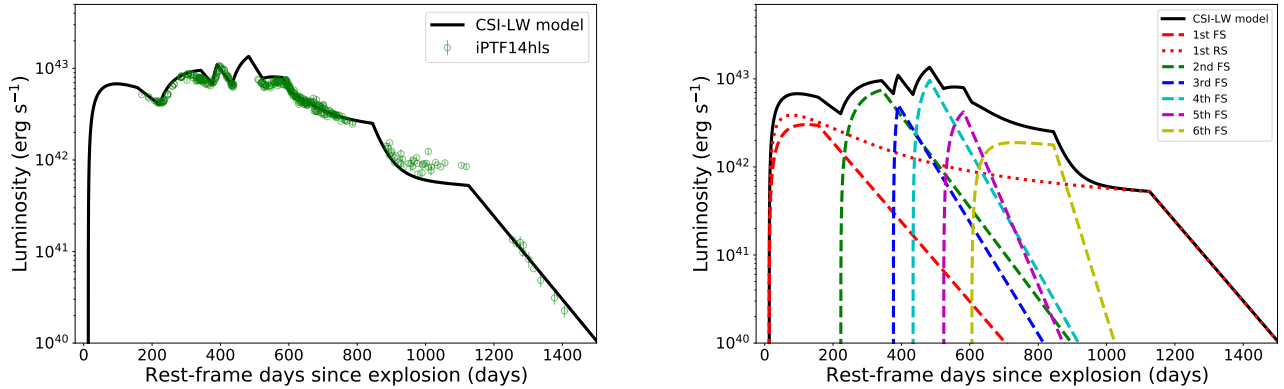


Figure 2. Fit to the bolometric luminosity (left panel) of iPTF14hls by the CSI-LW model. The contributions from forward shocks and reverse shocks of i th CSM are plotted in right panel. FS emission is plotted in dashed lines, while the first RS is plotted in the red dotted line.

Table 2. Model parameters with the CSI plus ^{56}Ni model.

| ejecta properties | | | | | | |
|--|------|------|-----|------|------|-------|
| $M_{\text{ej}}(M_{\odot})$ | 86 | | | | | |
| $M_{\text{Ni}}(M_{\odot})$ | 0.9 | | | | | |
| $v_{\text{SN}}(\text{km s}^{-1})$ | 5200 | | | | | |
| δ | 0 | | | | | |
| n | 7 | | | | | |
| CSM properties | | | | | | |
| | 1st | 2nd | 3rd | 4th | 5th | 6th |
| $M_{\text{CSM}}(M_{\odot})$ | 18 | 15 | 25 | 20 | 35 | 80 |
| $R_{\text{in}}(10^{15} \text{ cm})$ | 8.4 | 14.8 | 18 | 21 | 23 | 26 |
| $\rho_{\text{in}}(10^{-15} \text{ g cm}^{-3})$ | 8.5 | 7.3 | 5.4 | 5.2 | 4.1 | 1.1 |
| ϵ_{FS} | 0.07 | 0.14 | 0.1 | 0.08 | 0.04 | 0.018 |
| ϵ_{RS} | 0.26 | 0 | 0 | 0 | 0 | 0 |

exponential decline starting on ~ 1100 days post explosion (see Figure 2) because the large total mass ($M_{\text{ej}} + \sum M_{\text{CSMs}}$) results in a shallow exponential decline.

Based on above considerations, we explore the possibility of fitting the initial decline of the light curve by ^{56}Ni decay. The fitting result is presented in Figure 3, with the fitting parameters listed in the Table 2. The gray opacity to ^{56}Ni cascade decay photons is $\kappa_{\gamma} = 0.027 \text{ cm}^2 \text{ g}^{-1}$ (Colgate et al. 1980; Swartz et al. 1995). In this model, the explosion energy is very close to the value given in Equation (13).

It is found that the observed light curve around ~ 1000 days post explosion declines according to $L \propto t^{-0.3}$ (see Figure 3), while the theoretical light curve with $n = 7$ and $s = 2$ gives $L \propto t^{-0.6}$. This is the reason why there is some deviation between the theoretical light curve and observational data. Actually, $L \propto t^{-0.3}$ is consistent with $n = 12$ and $s = 2$. Such an outer density profile of the ejecta is expected for the envelopes of red supergiant progenitors, while $n = 7$ can be found in the envelopes of more compact progenitors (Matzner & McKee 1999; Chatzopoulos et al. 2012). This indicates that the outer density profile of the ejecta changes during the successive collisions with CSMs.

3. MASS LOSS HISTORY

Hereafter we consider the CSI-LW and CSI-LW plus ^{56}Ni models as our fiducial models. Given the fitting parameters listed in Table 1 and Table 2, mass loss history of iPTF14hls can be studied. Before the discovery of iPTF14hls on

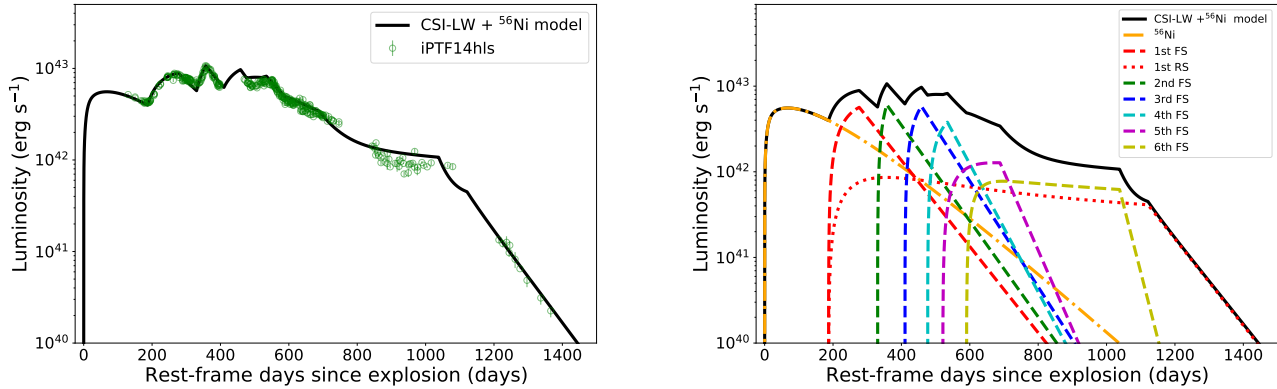


Figure 3. Fit to the bolometric luminosity (left panel) of iPTF14hls by the CSI-LW plus ^{56}Ni model. The contributions from FS, RS, and ^{56}Ni are plotted in right panel. FS emission are plotted in dashed lines, the first RS is plotted in the red dotted line, and ^{56}Ni contribution is plotted in the orange dashed-dotted line.

2014 Sep. 22, there is a historic eruption at the same position of iPTF14hls on 1954 Feb. 23 (Arcavi et al. 2017). Assuming that this eruption corresponds to the first CSM listed in Table 2, the wind velocity v_{wind} can be derived, namely $v_{\text{wind}} = R_{\text{out},1} (1+z) / 60.58 \text{ yr} \simeq 42 \text{ km s}^{-1}$, slightly higher than the observed wind velocity of Type II-P SNe (Smith 2014). Here R_{out} is the outer radius of the CSM that is calculated according to R_{in} , M_{CSM} and ρ_{in} . If the initial decline of the light curve is attributed to ^{56}Ni decay, the wind velocity is $v_{\text{wind}} \simeq 71 \text{ km s}^{-1}$. Based on these wind velocities, we list the mass loss history in Table 3.

Table 3. Mass loss history of iPTF14hls derived according to the CSI-LW and CSI-LW+ ^{56}Ni models.

| | | CSI-LW model | | | | | | CSI-LW plus ^{56}Ni model | | | | | |
|-----------------------|---------------------------------|--------------|-------|-------|-------|-------|-------|------------------------------------|------|------|------|-------|-------|
| | | 1st | 2nd | 3rd | 4th | 5th | 6th | 1st | 2nd | 3rd | 4th | 5th | 6th |
| \dot{M} | ($M_{\odot} \text{ yr}^{-1}$) | 0.37 | 0.6 | 1.3 | 1.3 | 1.2 | 1.0 | 0.85 | 2.3 | 2.5 | 3.3 | 3.1 | 1.0 |
| T_{start} | (yr) | 58.6 | 117.1 | 126.2 | 152.3 | 176.0 | 244.7 | 58.6 | 72.5 | 90.2 | 99.7 | 113.9 | 193.8 |
| T_{end} | (yr) | 4.5 | 75.0 | 120.0 | 133.5 | 157.5 | 176.3 | 37.4 | 65.9 | 80.2 | 93.5 | 102.4 | 115.8 |
| T_{duration} | (yr) | 54.1 | 42.1 | 6.2 | 18.7 | 18.5 | 68.4 | 21.2 | 6.6 | 10.1 | 6.2 | 11.5 | 78.0 |
| T_{waiting} | (yr) | 4.5 | 16.5 | 3.0 | 7.3 | 5.3 | 0.2 | 37.4 | 7.4 | 7.6 | 3.3 | 2.8 | 1.9 |
| E_{burst} | (10^{47} erg) | 3.6 | 4.5 | 1.4 | 4.4 | 3.9 | 12.4 | 9.1 | 7.5 | 12.6 | 10.1 | 17.6 | 40.3 |

Notes. \dot{M} is the mass loss rate, T_{start} , T_{end} , T_{duration} , T_{waiting} , and E_{burst} are the start time, end time, duration, waiting time, and burst energy of the mass loss episodes, respectively. All times are in rest frame of the host galaxy.

All timescales in Table 3 are calculated in the rest frame of the host galaxy of iPTF14hls with time zero point set on the discovery date of iPTF14hls². Mass loss rates are $\dot{M} \simeq 0.4 - 1.3 M_{\odot} \text{ yr}^{-1}$ (in the CSI-LW model) or $\dot{M} \simeq 0.85 - 3.3 M_{\odot} \text{ yr}^{-1}$ (in the CSI-LW plus ^{56}Ni model), slightly higher than that of Type II_n (Schlegel 1990; Filippenko 1997) and II_n-P SNe (e.g., Kiewe et al. 2012; Taddia et al. 2013; Smith 2014).

In Table 3 we also list the outburst energy for each mass-loss episode, calculated according to $E_{\text{burst}} = \frac{1}{2} M_{\text{CSM}} v_{\text{wind}}^2$. The burst energies have a typical value of $10^{47} - 10^{48} \text{ erg}$. These derived burst energies are small compared to the gravitational binding energies (see Equation 14 below) of the CSM-shells before ejection. This indicates that there could be much more energy-release episodes during the final evolution of the progenitor, of which only a fraction of the energy-release episodes trigger large-scale mass loss.

² A more appropriate zero point time may be the explosion time of iPTF14hls. However, given the large uncertainty of the explosion time, here we just use the discovery date. This approximation only introduces a very minor error in the derived quantities.

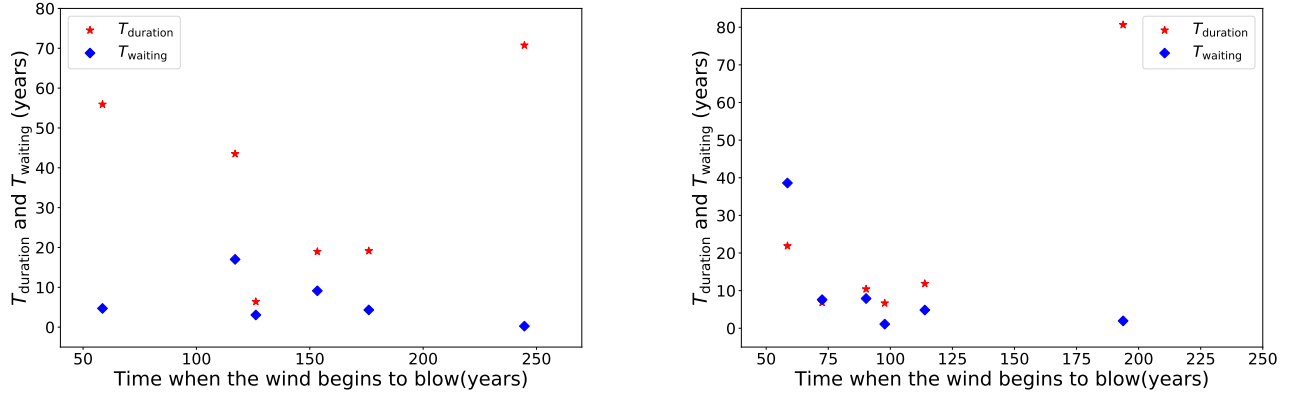


Figure 4. The waiting time and duration of the mass-loss episodes in the CSI-LW (left panel) and CSI-LW+ ^{56}Ni (right panel) models.

Waiting times are calculated as $T_{\text{waiting},i} = T_{\text{end},i} - T_{\text{start},i-1}$ for the i th CSM. The duration and waiting time of the mass-loss episodes are presented in Figure 4. From Figure 4, we see that during the final 200 years of evolution of the progenitor of iPTF14hls, mass loss is very frequent, with only very short quiescence periods (waiting times) following the longer wind blowing episodes. An interesting exception is the last mass-loss episode (corresponding to the first CSM) in the CSI-LW+ ^{56}Ni model, where the waiting time $T_{\text{waiting}} = 37.4\text{yr}$ is longer than the duration $T_{\text{duration}} = 21.2\text{yr}$. This waiting time is also much longer than the waiting times of earlier mass-loss episodes, which have values $T_{\text{waiting}} = 1.9 - 7.6\text{yr}$ (see Figure 4 and Table 3). If the CSI-LW+ ^{56}Ni model is correct, this indicates that there could be a long quiescence before the final collapse of the progenitor.

It should be mentioned that the wind velocity is expected to increase as the progenitor becomes more and more compact via shedding a large fraction of its mass. Taking this fact into account, the mass loss rates of the earlier mass-loss episodes (the second to sixth CSMs listed in Table 3) could be lower and the duration and waiting time could be longer than the values given in Table 3. It is also possible that one or more of the CSM-shells are the merging results with the late fast-moving shell running into the earlier slow-moving shell.

4. DISCUSSION AND CONCLUSIONS

The derived main-sequence mass ($M_{\text{zams}} \simeq 245.5M_{\odot}$) is consistent with a pair-instability supernova (PISN; Barkat et al. 1967; Rakavy & Shaviv 1967; Ober et al. 1983; Bond et al. 1984; Glatzel et al. 1985; Scannapieco et al. 2005; Kasen et al. 2011), which has a mass range $140M_{\odot} < M_{\text{zams}} < 260M_{\odot}$. However, theoretical studies suggest that massive stars with $M_{\text{zams}} \simeq 245.5M_{\odot}$ will end their lives during the final explosions that disrupt themselves completely and do not episodically lose mass. In this case the CSM-shells listed in Table 2 may be generated by envelope instabilities (Yoon & Cantiello 2010; Owocki 2015), which is suggested for the mass loss of some Type II-P SNe in their final evolution stage (e.g., Rui et al. 2019). Another difficulty for the interpretation of iPTF14hls as a PISN is that the derived ^{56}Ni mass $M_{\text{Ni}} = 0.9M_{\odot}$ (see Table 2) in the CSI-LW+ ^{56}Ni model is lower than the expected yield of ^{56}Ni during the final disruptive explosion of a PISN, which could have $M_{\text{Ni}} \sim 50M_{\odot}$ for a $M_{\text{zams}} \simeq 250M_{\odot}$ star (Heger & Woosley 2002; Umeda & Nomoto 2002).

The properties of the progenitor of iPTF14hls are more consistent with a pulsational pair-instability supernova³ (PPISN; Barkat et al. 1967; Woosley et al. 2007; Chen et al. 2014; Woosley & Heger 2015), as discussed in the literature (Arcavi et al. 2017; Woosley 2018). There may be some overlap between the initial mass of a star that will end up as a PISN or PPISN, which has a mass range $70M_{\odot} < M_{\text{zams}} < 140M_{\odot}$. This is plausible because our current understanding of massive star evolution is incomplete owing to the complex physics involved, including metallicity-related mass loss, chemical mixing, rotation, binary-interaction-related mass transfer, and magnetic torques (Ohkubo et al. 2009; Chatzopoulos & Wheeler 2012; Woosley 2017, 2019; Leung et al. 2019; Marchant et al. 2019). Indeed, Yoshida et al. (2016) calculated the evolution of stars with metallicity $Z = 0.004$ and initial masses of 140, 200, and

³ Because of mass loss, the metallicity of the progenitor of iPTF14hls should be $Z \leq 0.5Z_{\odot}$ (Langer et al. 2007; Georgy et al. 2013; Yusof et al. 2013; Spera et al. 2015; Leung et al. 2019) to form He core massive enough to undergo pulsational pair-instability. This results in an opacity κ essentially identical to our adopted value because electron scattering opacity depends on metallicity very weakly.

$250M_{\odot}$, which are well within the usually assumed mass range of PISNe. They found their masses decrease to 54, 59, and $61M_{\odot}$ before the neon burning owing to mass loss. Eventually, the above three stars experience six ($M = 140M_{\odot}$) to three ($M = 250M_{\odot}$) episodes of mass loss induced by PPI during their final 1 ($M = 140M_{\odot}$) to 1400 ($M = 250M_{\odot}$) yr evolution before core collapse.

For a star that will end up as a PPISN, electron–positron pairs will be generated when the central temperature of the massive helium core rises to $(1.8 - 2.3) \times 10^9$ K (Fowler & Hoyle 1964; Barkat et al. 1967; Rakavy & Shaviv 1967). Sudden loss of pressure due to the production of electron–positron pairs leads to the contraction of the helium core. Then explosive burning of oxygen ensues so as to eventually reverse the contraction of the core to expansion. Such pulsational activity becomes more and more energetic to shed some amount of envelope during the final evolution of a PPISN progenitor. The duration of pulsational activity spans a wide range of time, from a few hours to 10^4 yr (Woosley 2017), in accord with the mass loss history listed in Table 3.

During the pair pulsation, the progenitor of a PPISN may be a red supergiant (RSG), a blue supergiant (BSG), a luminous blue variable, or Wolf–Rayet star if the hydrogen envelope is completely shed away by continuous mass loss (Woosley 2017). The gravitational binding energy of the hydrogen shell that will be blown away by the pulsation is

$$E_p = 1.2 \times 10^{49} \text{ erg} \left(\frac{M_R}{150M_{\odot}} \right) \left(\frac{M_s}{30M_{\odot}} \right) \left(\frac{R_p}{10^{14} \text{ cm}} \right)^{-1}, \quad (14)$$

where M_s is the shell mass that will be blown away, M_R is the mass left over after mass shedding, R_p is the radius of the progenitor star during helium burning. $R_p \approx 10^{14}$ cm if the progenitor star is a RSG, while $R_p \approx 10^{13}$ cm for a BSG. The progenitor of iPTF14hls is likely an RSG since the above binding energy is closer to the burst energies listed in Table 3. Owing to the same reason, the initial decline of the light curve could be more likely attributed to ^{56}Ni decay since in the CSI-LW+ ^{56}Ni model the burst energies is closer to the binding energy.

The amount of ^{16}O burnt during one pulsation can be estimated as

$$M_{\text{O}} = 0.01M_{\odot} \left(\frac{E_p}{10^{49} \text{ erg}} \right). \quad (15)$$

Here the energy release by ^{16}O burning is 0.52 MeV per nucleon (Arnett 1996; Wallerstein et al. 1997). The contraction timescale of the helium core is the dynamical timescale. Therefore such an amount of ^{16}O will be burnt in

$$t_d = 3.8 \text{ hr} \left(\frac{R_c}{10^{12} \text{ cm}} \right)^{3/2} \left(\frac{M_c}{50M_{\odot}} \right)^{-1/2}, \quad (16)$$

where R_c and M_c are the radius and mass of the helium core that participates in the pulsation. The timescales of mass ejection and subsequent resettlement to a new bound state are the Kelvin–Helmholtz timescale, i.e., several years (see Table 3), which is much longer than the dynamical timescale given by Equation (16).

It is usually assumed that the remnants of PPISNe are massive black holes and no ^{56}Ni is ejected to power the SN light curve (e.g., Woosley 2017; Leung et al. 2019). Tolstov et al. (2017), on the other hand, propose that a PPISN can eject a large amount of ^{56}Ni ($M_{\text{Ni}} = 6M_{\odot}$) to power the light curve of SLSN PTF12dam, despite the formation of a black hole in PTF12dam. Given the moderate amount of ^{56}Ni in the CSI-LW+ ^{56}Ni model (see Table 2), we suggest that the ^{56}Ni may be ejected during the collapse of the helium core to a massive black hole, i.e., a collapsar (Woosley 1993). This implies a rapid rotation of the helium core. However, such a rapid rotation is in tension with the existence of the hydrogen-rich envelope of the progenitor of iPTF14hls since rotation tends to remove the hydrogen envelope. This tension can be relaxed by assuming a differential rotation of the progenitor star. The derived explosion energy (Equation 13) is also consistent with the collapsar model.

To date, there are several candidates for PPISNe (Ben-Ami et al. 2014; Lunnan et al. 2018; Gomez et al. 2019). Nicholl et al. (2020) reported the detection of a Type IIIn SLSN 2016aps with energy $E_{\text{SN}} \gtrsim 10^{52}$ erg and a total mass (ejecta + CSM) exceeding $50 - 100M_{\odot}$. Detailed one-dimensional radiation-hydrodynamic simulations (Suzuki et al. 2021) suggest that SN 2016aps could be a collision of an ejecta mass $M_{\text{ej}} = 30M_{\odot}$ with a $M_{\text{CSM}} \simeq 8M_{\odot}$ wind-like CSM of outer radius 10^{16} cm. SN 2016aps has a radiated energy $E_{\text{rad}} \gtrsim 5 \times 10^{51}$ erg, which is an order of magnitude higher than iPTF14hls. The mass loss rate of SN 2016aps, $\dot{M} \approx 0.3M_{\odot} \text{ yr}^{-1}$, assuming a wind velocity $u_w = 100 \text{ km s}^{-1}$, is comparable to that of iPTF14hls. Yang et al. (2021) reported the Type II SN 2020faa, whose first six months of light curves are of great similarity with those of iPTF14hls.

The light curve of iPTF14hls is very unusual among SNe studied so far. In this paper, we explore the possibility of interpreting iPTF14hls as a multiple interaction-powered SN. We find that within reasonable parameters, the theoretical light curve matches well with the light curve of iPTF4hls. This makes iPTF14hls a possible candidate for PPISN. [Moriya et al. \(2020\)](#) proposed that iPTF14hls is produced by a continuous outflow like a stellar wind rather than a mass ejection. They calculated the mass-loss rates of iPTF14hls as high as $10M_{\odot}\text{yr}^{-1}$ in the bright phase. Such an extreme mass loss rate is much higher than the results obtained from our calculations. [Dessart \(2018\)](#) found magnetar-powered SN ejecta reproduces some the observed properties of iPTF14hls, including the sustained brightness in the R band, the blue optical color, and the broad HI lines. However, the magnetar model is difficult to produce fluctuating light curves with multiple peaks, unless consider variable thermal energy injection from magnetar spin down ([Moriya et al. 2022](#)). In the future, more observations and improved theoretical modelings can improve our understanding of very massive stars ([Heger et al. 2003](#)).

We thank the anonymous referee for his/her constructive comments that allow us to improve the paper significantly. We also thank Iair Arcavi and Jesper Sollerman for providing us the observational data. This work is supported by the National Program on Key Research and Development Project of China (Grant Nos. 2021YFA0718500 and 2017YFA0402600), and the National Natural Science Foundation of China (Grant Nos. U1938201, 11833003, 12103055). X.F. Wang is supported by the National Natural Science Foundation of China (NSFC grants 12033003 and 11633002), the Major State Basic Research Development Program (grant 2016YFA0400803), and the Scholar Program of Beijing Academy of Science and Technology (DZ:BS202002).

REFERENCES

- Andrews, J. E., & Smith, N. 2018, *MNRAS*, 477, 74
- Arnett, W. D. 1982, *ApJ*, 253, 785
- Arnett, D. 1996, *Supernovae and Nucleosynthesis: An Investigation of the History of Matter from the Big Bang to the Present* (Princeton, NJ: Princeton Univ. Press), 112
- Arcavi, I., Howell, D. A., Kasen, D., et al. 2017, *Natur*, 551, 210
- Barkat, Z., Rakavy, G., & Sack, N. 1967, *PhRvL*, 18, 379
- Ben-Ami, S., Gal-Yam, A., Mazzali, P. A., et al. 2014, *ApJ*, 785, 37
- Bond, J. R., Arnett, W. D., & Carr, B. J. 1984, *ApJ*, 280, 825
- Bruch, R. J., Gal-Yam, A., Schulze, S., et al. 2021, *ApJ*, 912, 46
- Chatzopoulos, E., & Wheeler, J. C. 2012, *ApJ*, 748, 42
- Chatzopoulos, E., Wheeler, J. C., & Vinko, J. 2012, *ApJ*, 746, 121
- Chen, K.-J., Woosley, S., Heger, A., Almgren, A., & Whalen, D. J. 2014, *ApJ*, 792, 28
- Chevalier, R. A. 1982, *ApJ*, 258, 790
- Chevalier, R. A., & Fransson, C. 1994, *ApJ*, 420, 268
- Chugai, N. N. 2018, *AstL*, 44, 370
- Chugai, N. N., & Danziger, I. J. 1994, *MNRAS*, 268, 173
- Colgate, S. A., Petschek, A. G., & Kriese, J. T. 1980, *ApJL*, 237, L81
- Dessart, L. 2018, *A&A*, 610, L10
- Filippenko, A. V. 1997, *ARA&A*, 35, 309
- Fowler, W. A., & Hoyle, F. 1964, *ApJS*, 9, 201
- Gal-Yam, A. 2012, *Sci*, 337, 927
- Gal-Yam, A. 2019, *ARA&A*, 57, 305
- Gal-Yam, A., Arcavi, I., Ofek, E. O., et al. 2014, *Natur*, 509, 471
- Gal-Yam, A., Bruch, R., Schulze, S., et al. 2022, *Natur*, 601, 201
- Georgy, C., Ekström, S., Eggenberger, P., et al. 2013, *A&A*, 558, A103
- Glatzel, W., Fricke, K. J., & El Eid, M. F. 1985, *A&A*, 149, 413
- Gofman, R. A., & Soker, N. 2019, *MNRAS*, 488, 5854
- Gomez, S., Berger, E., Nicholl, M., et al. 2019, *ApJ*, 881, 87
- Heger, A., Fryer, C. L., Woosley, S. E., et al. 2003, *ApJ*, 591, 288
- Heger, A., & Woosley, S. E. 2002, *ApJ*, 567, 532
- Hosseinzadeh, G., Berger, E., Metzger, B. D., et al. 2021, *arXiv:2109.09743*
- Hosseinzadeh, G., Valenti, S., McCully, C., et al. 2018, *ApJ*, 861, 63
- Inserra, C. 2019, *NatAs*, 3, 697
- Jacobson-Galán, W. V., Dessart, L., Jones, D. O., et al. 2022, *ApJ*, 924, 15
- Kaplan, N., & Soker, N. 2020, *MNRAS*, 492, 3013
- Kasen, D., Woosley, S. E., & Heger, A. 2011, *ApJ*, 734, 102
- Khazov, D., Yaron, O., Gal-Yam, A., et al. 2016, *ApJ*, 818, 3

- Kiewe, M., Gal-Yam, A., Arcavi, I., et al. 2012, *ApJ*, 744, 10
- Langer, N., Norman, C. A., de Koter, A., et al. 2007, *A&A*, 475, L19
- Leung, S.-C., Blinnikov, S., Nomoto, K., et al. 2020, *ApJ*, 903, 66
- Leung, S.-C., Fuller, J., & Nomoto, K. 2021, *ApJ*, 915, 80
- Leung, S.-C., Nomoto, K., & Blinnikov, S. 2019, *ApJ*, 887, 72
- Li, L., Wang, S. Q., Liu, L. D., et al. 2020, *ApJ*, 891, 98
- Li, W. X., Wang, X. F., & Zhang, T. M. 2015, *ATel*, 6898
- Liu, L.-D., Wang, L.-J., & Gao, H. 2020, *Research Notes of the American Astronomical Society*, 4, 162
- Liu, L. D., Wang, L. J., Wang, S. Q., & Dai, Z. G. 2018, *ApJ*, 856, 59
- Liu, T., Song, C.-Y., Yi, T., Gu, W.-M., & Wang, X.-F. 2019, *JHEAp*, 22, 5
- Lunnan, R., Fransson, C., Vreeswijk, P. M., et al. 2018, *NatAs*, 2, 887
- Marchant, P., Renzo, M., Farmer, R., et al. 2019, *ApJ*, 882, 36
- Matzner, C. D., & McKee, C. F. 1999, *ApJ*, 510, 379
- Modjaz, M., Gutiérrez, C. P., & Arcavi, I. 2019, *NatAs*, 3, 717
- Moriya, T. J., Blinnikov, S. I., Tominaga, N., et al. 2013a, *MNRAS*, 428, 1020
- Moriya, T. J., Murase, K., Kashiyama, K., et al. 2022, *MNRAS* in press, arXiv:2202.03082
- Moriya, T. J., Maeda, K., Taddia, F., et al. 2013b, *MNRAS*, 435, 1520
- Moriya, T. J., Mazzali, P. A., & Pian, E. 2020, *MNRAS*, 491, 1384
- Moriya, T. J., Sorokina, E. I., & Chevalier, R. A. 2018, *SSRv*, 214, 59
- Nicholl, M., Blanchard, P. K., Berger, E., et al. 2020, *NatAs*, 4, 893
- Ober, W. W., El Eid, M. F., & Fricke, K. J. 1983, *A&A*, 119, 61
- Ohkubo, T., Nomoto, K., Umeda, H., Yoshida, N., & Tsuruta, S. 2009, *ApJ*, 706, 1184
- Owocki, S. P. 2015, in *Astrophysics and Space Science Library*, Vol. 412, *Very Massive Stars in the Local Universe*, ed. J. S. Vink (Cham: Springer), 113
- Parker, E. N. 1961, *ApJ*, 133, 1014
- Pellegrino, C., Howell, D. A., Vinkó, J., et al. 2022, *ApJ*, 926, 125
- Quimby, R. M., Kulkarni, S. R., Kasliwal, M. M., et al. 2011, *Natur*, 474, 487
- Quimby, R. M., Wheeler, J. C., Höflich, P., et al. 2007, *ApJ*, 666, 1093
- Rakavy, G., & Shaviv, G. 1967, *ApJ*, 148, 803
- Rui, L. M., Wang, X. F., Mo, J., et al. 2019, *MNRAS*, 485, 1990
- Scannapieco, E., Madau, P., Woosley, S., Heger, A., & Ferrara, A. 2005, *ApJ*, 633, 1031
- Schlegel, E. M. 1990, *MNRAS*, 244, 269
- Smith, N. 2014, *ARA&A*, 52, 487
- Smith, N. 2017, in *Interacting Supernovae: Types IIin and Ibn*, ed. A. W. Alsabti & P. Murdin (Cham: Springer International), 403
- Soker, N., & Gilkis, A. 2018, *MNRAS*, 475, 1198
- Sollerman, J., Taddia, F., Arcavi, I., et al. 2019, *A&A*, 621, A30
- Spera, M., Mapelli, M., & Bressan, A. 2015, *MNRAS*, 451, 4086
- Suzuki, A., Moriya, T. J., & Takiwaki, T. 2019, *ApJ*, 887, 249
- Suzuki, A., Nicholl, M., Moriya, T. J., & Takiwaki, T. 2021, *ApJ*, 908, 99
- Swartz, D. A., Sutherland, P. G., & Harkness, R. P. 1995, *ApJ*, 446, 766
- Taddia, F., Stritzinger, M. D., Sollerman, J., et al. 2013, *A&A*, 555, A10
- Tolstov, A., Nomoto, K., Blinnikov, S., et al. 2017, *ApJ*, 835, 266
- Tolstov, A., Nomoto, K., Sorokina, E., et al. 2019, *ApJ*, 881, 35
- Umeda, H., & Nomoto, K. 2002, *ApJ*, 565, 385
- Uno, K., & Maeda, K. 2020, *ApJ*, 897, 156
- van Marle, A. J., Smith, N., Owocki, S. P., & van Veelen, B. 2010, *MNRAS*, 407, 2305
- Wallerstein, G., Iben, I. Jr., Parker, P., et al. 1997, *RvMP*, 69, 995
- Wang, L. J., Wang, X. F., Wang, S. Q. et al., 2018, *ApJ*, 865, 95
- Wang, L. J., Wang, X. F., Cano, Z., et al. 2019a, *MNRAS*, 489, 1110
- Wang, L. J., & Yu, H. 2022, *CatFit: Calculate the bolometric luminosity of an SN with multiple ejecta-CSM interactions*, v1.0.0, Zenodo, doi:10.5281/zenodo.6508082
- Wang, S. Q., Gan, W.-P., Li, L. et al. 2019b, arXiv:1904.09604
- Wang, S. Q., Liu, L. D., Dai, Z. G., Wang, L. J., & Wu, X. F. 2016, *ApJ*, 828, 87
- Wheeler, J. C., Chatzopoulos, E., Vinkó, J., et al. 2017, *ApJL*, 851, L14
- Woosley, S. E. 1993, *ApJ*, 405, 273
- Woosley, S. E. 2017, *ApJ*, 836, 244
- Woosley, S. E. 2018, *ApJ*, 863, 105
- Woosley, S. E. 2019, *ApJ*, 878, 49

- Woosley, S. E., Blinnikov, S., & Heger, A. 2007, *Natur*, 450, 390
- Woosley, S. E., & Heger, A. 2015, in *Astrophysics and Space Science Library*, Vol. 412, *Very Massive Stars in the Local Universe*, ed. J. S. Vink (Cham: Springer), 199
- Xiang, D. F., Wang, X. F., Lin, W. L., et al. 2021, *ApJ*, 910, 42
- Yang, S., Sollerman, J., Chen, T. -W., et al. 2021, *A&A*, 646, A22
- Yaron, O., Perley, D. A., Gal-Yam, A., et al. 2017, *NatPh*, 13, 510
- Yoon, S.-C., & Cantiello, M., 2010, *ApJL*, 717, L62
- Yoshida, T., Umeda, H., Maeda, K., & Ishii, T. 2016, *MNRAS*, 457, 351
- Yuan, Q., Liao, N. H., Xin, Y. L., et al. 2018, *ApJL*, 854, L18
- Yusof, N., Hirschi, R., Meynet, G., et al. 2013, *MNRAS*, 433, 1114